

See discussions, stats, and author profiles for this publication at: <https://www.researchgate.net/publication/234119132>

Polymers as Templates for Au and Au@Ag Bimetallic Nanorods: UV–Vis and Surface Enhanced Raman Spectroscopy

ARTICLE in CHEMISTRY OF MATERIALS · DECEMBER 2012

Impact Factor: 8.35 · DOI: 10.1021/cm3031329

CITATIONS

30

READS

107

8 AUTHORS, INCLUDING:



Rafael Contreras

University of Malaga

22 PUBLICATIONS 470 CITATIONS

SEE PROFILE



Petr Formanek

Leibniz Institute of Polymer Research Dresden

63 PUBLICATIONS 752 CITATIONS

SEE PROFILE



Dieter Fischer

Leibniz Institute of Polymer Research Dresden

67 PUBLICATIONS 946 CITATIONS

SEE PROFILE



Petra Uhlmann

Leibniz Institute of Polymer Research Dresden

83 PUBLICATIONS 1,179 CITATIONS

SEE PROFILE

Polymers as Templates for Au and Au@Ag Bimetallic Nanorods: UV–Vis and Surface Enhanced Raman Spectroscopy

Rafael Contreras-Caceres,[†] Claudine Dawson,^{†,‡} Petr Formanek,[†] Dieter Fischer,[†] Frank Simon,[†] Andreas Janke,[†] Petra Uhlmann,^{*,†} and Manfred Stamm^{†,‡}[†]Leibniz-Institut für Polymerforschung, Dresden e.V. Hohe Strasse 6, 01069 Dresden, Germany[‡]Technische Universität Dresden, Department of Chemistry and Food Chemistry, 01062 Dresden, Germany

ABSTRACT: In this study, we report on the fabrication of nanoassemblies composed by Au and bimetallic core–shell Au@Ag nanorods immobilized onto pH-responsive poly(2-vinylpyridine) (P2VP) brushes. The general process includes the synthesis of gold nanorods (through the seed mediated method) and a subsequent reduction of AgNO₃ on the gold surface. These colloidal particles were immobilized onto carboxy-terminated P2VP brushes (COOH-P2VP), previously grafted on underlying substrates (silicon wafers and glass slides). UV–vis spectroscopy and transmission electron microscopy (TEM) images confirmed the morphology of the gold nanorods and the core–shell structure of the bimetallic Au@Ag nanorods. The presence of metal nanoparticles on the P2VP-functionalized substrates was demonstrated by atomic force microscopy (AFM), X-ray photoelectron spectroscopy (XPS), and scanning electron microscopy (SEM) images. The swelling–deswelling behavior of the pH responsive polymer brushes was confirmed using UV–vis spectroscopy over P2VP brushes functionalized glass slides with immobilized gold nanorods (P2VP–Au rod) at two different pH values. A significant displacement of 32 nm in the longitudinal plasmon band was observed between the swollen and the collapsed state of the pH-sensitive polymer brushes, proving the potential application of these nanostructures for the fabrication of pH nanosensors capable of detect changes in the pH of aqueous media. The surface enhanced Raman spectroscopy (SERS) activity of the nanoassemblies was demonstrated using a dye molecule, rhodamine 6G (R6G), as model analyte. The remarkable SERS intensity of silver compared to gold was confirmed. In addition, the SERS signal intensity depended on both the concentration of particles deposited on the functionalized substrate and the thickness of the silver shell surrounding the gold nanorod. Enhancement factors (EFs) on the order of 10¹¹ for immobilized Au@Ag nanoparticles demonstrated the ability of this novel nanostructured system for applications in the detection of conventional SERS analytes and offer the possibility to fabricate stable macroscopic devices for SERS spectroscopy applications.

KEYWORDS: metal nanoparticles, Au@Ag nanoparticles, pH-sensitive polymer brushes, plasmon displacement, SERS spectroscopy

1. INTRODUCTION

The attachment of metal nanoparticles over certain surfaces has received widespread attention during the last years due to the possibility to include metal nanoparticle properties into macroscopic 2D and 3D structures. These structures are especially interesting for biological and optical sensing,¹ cancer treatment,² catalysis,³ and various specialized photonic and electronic devices.⁴ Metal nanoparticles exhibit beautiful optical colors and possess remarkable spectroscopic properties due to the well-known localized surface plasmon resonance.^{5,6} This effect is produced when an external electromagnetic field interacts with the electron cloud of a metal particle, the diameter of which is between 1 and 100 nm. This phenomenon produces two important effects: (i) an intense absorption band in the UV–vis region of the electromagnetic spectrum, promoting important optical properties,⁷ and (ii) an increase in the local electromagnetic field near the nanoparticle surface, producing an enhancement in the Raman signal of certain analytes. The optical properties of metal nanoparticles were

theoretically explained by Gustav Mie in 1908.⁷ He solved the Maxwell's equation for metal spheres with a size smaller than the wavelength of the light. Mie's theory predicts that the optical properties of metal nanoparticles depend on several factors as particle size, type of material, or refractive index surrounding the metal nanoparticle. On the contrary, the SERS effect was discovered by Martin Fleischmann in 1974 and consists in an enormous enhancement of the Raman signal for molecules adsorbed on roughened metallic surfaces.^{8,9} This increase has been exploited during the last decades for surface enhanced Raman spectroscopy (SERS) applications.

Metal nanoparticle suspensions are attractive systems widely used as SERS substrates, because principally they can be prepared with a high reproducibility while being relatively inexpensive. Numerous metal colloidal suspensions were used,

Received: September 27, 2012

Revised: December 17, 2012

including gold and copper; however, silver is the most popular one since Ag nanoparticles have by far the strongest plasmon resonance because of their higher energy of the interband transition (~ 3.2 eV),¹⁰ relative to the energy of the plasmon resonance, leads to minimum damping of the plasmon. One important disadvantage of metal colloidal suspensions is that they are prone to agglomeration and a final sedimentation. For this reason, nowadays, the development of easy and reproducible methods to stabilize and immobilize metal nanoparticles in matrices or at substrates is an attractive and promising way to fabricate stable devices aiming expansions of the applications to macroscopic structures. In the last decades, a great number of methods and strategies for a successful immobilization of metal nanoparticles on certain substrates have been developed: among others, electron-beam lithography,^{11,12} block copolymer micelle nanolithography (BCML),¹³ in situ nucleation and growth,¹⁴ ion exchange process,^{15,16} layer by layer deposition,^{17,18} or self-assembled monolayers (SAMs).^{19,20} In many of these cases, the nano-assemblies are formed by gold or silver nanoparticles with fractal structures, such as particle aggregates or thin films, which form metallic islands. Within these aggregates, the oscillating localized surface plasmon is coupled between particles, this interparticle interaction via overlapping of evanescent fields is known as plasmon coupling²¹ and causes significant changes in the particle properties. The most important effect in those areas is that there is an extremely high SERS enhancement.^{8,22} Plasmon coupling is produced when the particle range spans between zero interparticle distance (the particles are in direct contact), at which plasmon coupling is the strongest, and the interparticle distance exceeding ~ 2.5 times the particle size, at which the particle behaves as essentially isolated.²³ The plasmon coupling of metal nanoparticles has been broadly exploited during the last years for optical, spectroscopic, and analytical applications.^{24–26}

Apart from the above-mentioned methods for the immobilization of metal nanoparticles on different surfaces, nowadays, the attachment of metal nanoparticles onto polymer brushes (which refers to a dense layer of polymer chains that are grafted irreversibly by one end to a surface)^{27,28} has turned in an important and promising alternative for the immobilization of metal nanoparticles on macroscopic surfaces exploiting the great number of advantages that polymer brushes offer over other conventional methods.²⁹ One of the most important differences with the above-mentioned methods is that polymer brushes can act as stimuli-responsive surfaces, responding to changes of temperature, solvent polarity, pH, and other stimuli, generally by reversible swelling–deswelling behavior.³⁰ As a result, a polymer brush provides an attractive platform for building plasmonic sensing devices owing to significant conformational changes in the polymer chains. Earlier studies demonstrate that polymer brushes serve as a perfect template for the preparation, immobilization, and stabilization of colloidal nanoparticles. For example, Liu et al.³¹ deposited gold nanocrystal on an attached polymer brushes configuration avoiding particle aggregation and obtaining elongated particle-rich domains. Spherical gold nanoparticles have been also immobilized on thermo-sensitive poly(*N*-isopropylacrylamide) (PNIPAM) brushes, particle aggregation was also avoided, resulting in the fabrication of temperature nanosensors, exploiting the temperature sensitive phase transition of this polymer at 32 °C, its lower critical solution temperature (LCST).³² Silver nanoparticles have been also attached onto

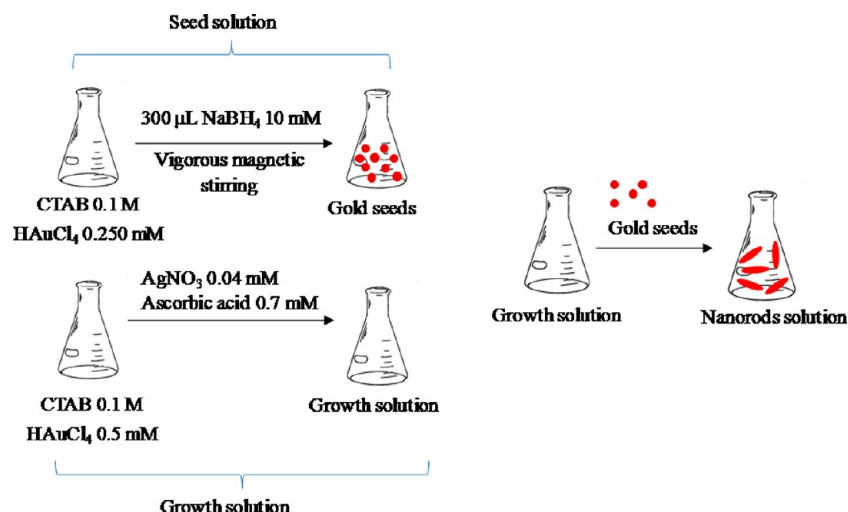
pH-responsive P2VP brushes, the global process involved the in situ synthesis of Ag nanoparticles via chemical reduction of silver nitrate in the presence of P2VP brushes.³³ This system was used to fabricate nanosensors for detecting the pH of surrounding aqueous media. Recently, Tokareva et al.³⁴ described the fabrication of a pH-sensitive nanodevice, which was composed of spherical gold nanoparticles deposited on P2VP brushes previously attached on Au nanoislands. This approach was exploited for transmission surface plasmon resonance (T-SPR) spectroscopy applications. They observed a remarkable 50 nm shift (to lower wavelength) by the swelling of P2VP polymer brushes caused by changing the pH from 5 to 2.

In this work, Au and core–shell Au@Ag nanorods were immobilized at pH-sensitive poly(2-vinylpyridine) (P2VP) polymer brushes, previously grafted on underlying substrates (silicon wafers and glass slides), with the aim to fabricate 2D devices containing both tunable optical responses, supplied by the gold nanorods, and enhanced SERS capabilities, provided by the Ag shell. We have included gold nanorods in the general structure instead of spherical morphologies due to the higher electromagnetic field concentration in nanorods compared with spheres,³⁵ so improved optical and spectroscopic responses were expected. This pH-responsive polymer brush possesses swelling–deswelling behavior in function of the local concentration of protons, changes in pH generate more charges inside the polymer brushes chains, which are then forced by electrostatic repulsion to stretch out and hence to swell to a thickness several times greater than that for the uncharged polymer.^{36–38} Improved tunable optical properties in function of pH and remarkable SERS intensities supplied by the core–shell Au@Ag nanostructures are conveniently demonstrated. Transmission electron microscopy images and UV–vis measurements were used to demonstrate the morphology of the synthesized Au nanorods and the core–shell bimetallic structure of the Au@Ag nanoparticles. UV–vis experiments, (performed over Au nanorods immobilized on P2VP brushes functionalized glass slides at two different pH values) showed a shift of 32 nm in the longitudinal plasmon band. This significant shift improves notably the possibilities for applications as a nanosensor for detecting the pH of surrounding aqueous medium compared with others morphologies.³²

Here, we also present our study on surface enhanced Raman spectroscopy (SERS). Rhodamine 6G (R6G) was chosen as dye molecule as a probe to evaluate the enhancement ability of the new metal nanoassemblies. The influence of the density of particles deposited on the polymer brushes in the SERS signal enhancement was investigated. Moreover, the high SERS activity of silver, compared to gold, was confirmed, and it was proportional to the thickness of the silver shell. Enhancement factors (EF) greater than 10^{11} were calculated for the Au@Ag specimens. These interesting results confirm that the used protocol is an easy and reproducible strategy for the fabrication of truly useful SERS substrates, which can be manufactured in large scale with low cost.

2. EXPERIMENTAL SECTION

Materials. Monocarboxy-terminated poly(2-vinylpyridine) (P2VP-COOH, $M_n = 40600$ g mol⁻¹) and poly(glycidyl methacrylate) (PGMA, $M_n = 17500$ g mol⁻¹), used as an adhesion promoter, were purchased from Polymer Source, Inc. (Canada). Tetrachloroauric acid (HAuCl₄·3H₂O), cetyltrimethyl ammonium bromide (CTAB), L-

Scheme 1. Seed Mediated Gold Nanorod Synthesis^a

^aThe gold seed particles are injected into the growth solution in the final step of the nanorod synthesis.

Table 1. Sample Used for the Experiments, Particle Dimension, Aspect Ratio (Length/Width), Concentration of the Particles during the Immobilization Process, Code Used, and Concentration of Rhodamine 6G in the SERS Experiments

sample	length, nm	width, nm	aspect ratio	[particle], mM	sample name	[R6G], mM
AuNrods	31.7 ± 2.9	11.2 ± 1.2	2.9 ± 0.4	0.5	Au0.5 mM	10 ⁻⁵
AuNrods	31.7 ± 2.9	11.2 ± 1.2	2.9 ± 0.4	1.5	Au1.5 mM	10 ⁻⁵
Au@Ag (R = 2)	35.4 ± 4.6	17.8 ± 3.2	2.0 ± 0.4	1.5	AuAg1	10 ⁻⁵
Au@Ag (R = 8)	36.9 ± 5.1	30.1 ± 4.9	1.3 ± 0.2	1.5	AuAg2	10 ⁻⁵

ascorbic acid, sodium borohydride (NaBH₄), and silver nitrate (AgNO₃) were purchased from Aldrich. Sodium hydroxide, Rhodamine 6G, and glycine ACS grade were supplied by Sigma. Highly polished single-crystal silicon wafers of {100} orientation with a native SiO₂ layer thickness of about 2 nm were obtained from Wacker Chemtronics (Germany) and used as substrates. Chloroform and ethanol were dried using standard methods before use. Millipore water was employed throughout the experiments.

Characterization Methods. The thicknesses of the grafted polymers brushes were measured using a SENTECH-402 (Sentech, Germany) at $\lambda = 632$ nm, and an incidence angle of 70°. The ellipsometric box model was used to follow the brush preparation steps.³⁹ The refractive indices used for the box model calculations were 3.858–0.018i, 1.4598, 1.525, and 1.595 for silicon substrate, native silica layer, PGMA layer, and P2VP brushes, respectively.

XPS studies were carried out by means of an AXIS ULTRA photoelectron spectrometer (Kratos Analytical, Manchester, UK). The spectrometer was equipped with a monochromatic Al K α ($h\nu = 1486.6$ eV) X-ray source of 300 W at 20 mA. The kinetic energy of the photoelectrons was determined with a hemispheric analyzer set to pass energy of 160 eV for the wide scan spectra and 20 eV for the high-resolution spectra. During all measurements, electrostatic charging of the sample was overcompensated by means of a low-energy electron source working in combination with a magnetic immersion lens. Later, all recorded peaks were shifted by the same amount which was necessary to set the C 1s peak to 285.00 eV for saturated hydrocarbons. Quantitative elemental compositions were determined from peak areas using experimentally determined sensitivity factors and the spectrometer transmission function. Spectrum background was subtracted according to Shirley. The high-resolution spectra were deconvoluted by means of a computer routine. Free parameters of component peaks were their binding energy, height, full width at half-maximum, and the Gaussian–Lorentzian ratio.

Atomic force microscopy (AFM) studies were performed with a Nanoscope IIIa-Multimode Microscope (Veeco, U.S.A.). Tapping

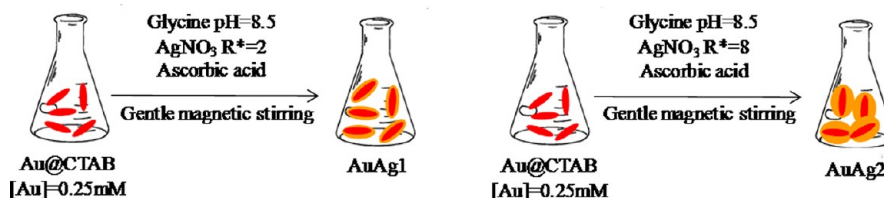
mode was used to map the film morphology under ambient conditions.

UV–vis measurements of aqueous colloidal solutions and for functionalized glass slide substrates were recorded with a Cary 50 spectrophotometer (Varian Analytical Instruments, Santa Clara CA, U.S.A.). For experiments on glass slide surfaces, the substrates were cut to a dimension of (4 × 1) cm. After treatment with gold nanorods the functionalized samples were introduced into a cleaned quartz cuvette and then filled with an aqueous solution at the respective pH value (pH 2 and pH 6). The UV–vis spectrum was taken after 2 min of immersion in each case. For the reference cuvette, a cleaned bare glass substrate (without brush layer and nanoparticles) was immersed into a solution of the same pH value.

Transmission electron microscopy (TEM) images of Au and Au@Ag nanorods were acquired on a Libra 200 microscope (Carl Zeiss AG, Oberkochen, Germany) operating at an acceleration voltage of 200 kV. Samples were prepared by drying a drop of 10 µL of colloidal suspension on a carbon-coated copper grid. Scanning electron microscopy (SEM) images were obtained using a Zeiss Ultra 55 Gemini (Carl Zeiss AG, Oberkochen, Germany) scanning electron microscope operating at 5.0 kV.

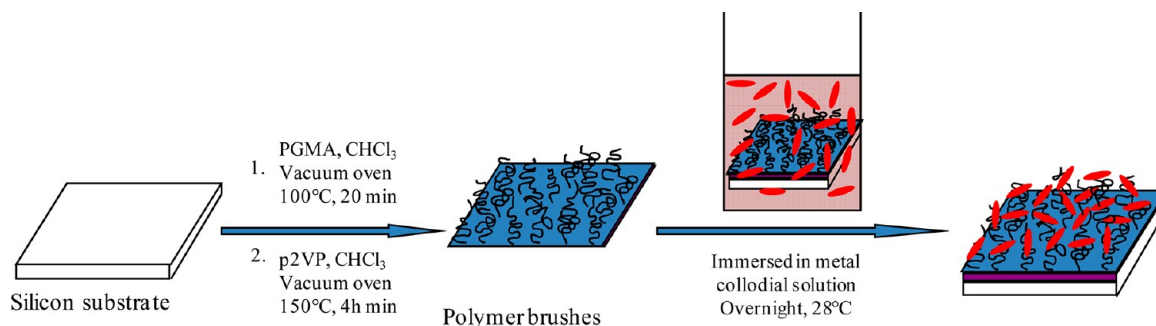
Raman and surface enhanced Raman spectroscopy (SERS) spectra were measured using a confocal Raman Microscope (CRM) alpha 300R, (WITec GmbH, Ulm, Germany). Raman and SERS signals were recorded by exciting the substrates with a laser power of 5 mW using a 532 nm laser line. All results were obtained in backscattering geometry using a 20× microscope objective. The SERS spectra were measured at different positions from the sample. For one Raman spectrum, between 50 and 200 single Raman spectra with a measuring time of 0.5 s were accumulated. Raman spectra were recorded within the spectral range of 0–2500 cm⁻¹ for Raman shift.

Synthesis of Gold Nanorods. The synthesis of Au nanorods was performed through a modification of the procedure published by Nikoobakht and El-Sayed.⁴⁰ Briefly, a seed solution was prepared as follows: In a 20 mL vial, 5 mL of an aqueous solution of HAuCl₄ (2.50 × 10⁻⁴ M) and cetyltrimethyl ammonium bromide CTAB (0.10 M)

Scheme 2. Silver Growth Process of Core–Shell Bimetallic Au@Ag Nanoparticles Using Two Different Amounts of AgNO_3 ^a

^aR* is the molar ratio between reduced Ag^+ and Au atoms in the Au nanorod solution.

Scheme 3. Schematic Representation of the Immobilization of Metal Nanoparticles onto the P2VP-Functionalized Substrates



was prepared at 28 °C; next, 0.3 mL of ice-cold freshly prepared 0.01 M NaBH_4 solution was added under vigorous magnetic stirring. The stirring was slowed down after 30 s, and the Au sol was gently stirred for 15 min at 40–45 °C to ensure removal of excess NaBH_4 . For the growth of gold nanorods, a growth solution was prepared containing $[\text{HAuCl}_4] = 5.00 \times 10^{-4}$ M, $[\text{CTAB}] = 0.1$ M, $[\text{AgNO}_3] = 4.00 \times 10^{-5}$ M at 28 °C. Next, 0.070 mL of 0.1 M ascorbic acid was added and mixed thoroughly. Finally, 0.15 mL of the seed solution was added. The procedure is summarized in Scheme 1. The dimensions of the obtained nanorod measured by TEM were 31.7 ± 2.9 nm \times 11.2 ± 1.2 nm with an aspect ratio of 2.9 ± 0.4 ; see Table 1.

Bimetallic Core–Shell Au@Ag Synthesis. Five milliliters of 0.5 mM gold nanorods solution previously prepared were centrifuged at 7500 rpm during 1 h to remove the CTAB excess, the supernatant was discarded, and the precipitate was redispersed in 5 mL of Milli-Q water. This colloidal suspension was used as seed solution to grow two different silver shells, denoted here as AuAg1 ($R = 2$) and AuAg2 ($R = 8$), where R is the molar ratio between reduced Ag^+ and Au atoms in the Au nanorod seeds, $R = [\text{Ag}^+]/[\text{Au}]$, see Table 1.

The growth process was carried out by using the method previously developed by Yang et al.⁴¹ Briefly, to 4.450 mL of 0.4 M glycine buffer solution at pH = 8.5 (adjusted with NaOH 1 M), 5 mL of the nanorod solution and 500 μL of AgNO_3 10 mM aqueous solution were added. Finally, 50 μL of ascorbic acid 100 mM were added under gentle magnetic stirring. After 10 min, the reduction was completed, and the used protocol is summarized in Scheme 2. The final bimetallic core–shell dimensions measured by TEM were 35.0 ± 4.6 nm \times 17.8 ± 3.2 nm with an aspect ratio of 2.0 ± 0.4 ; see Table 1.

With the aim to obtain a thicker silver shell, a modified growth process, as shown in Scheme 2, was performed. In this case, to 2.8 mL of 0.4 M glycine at pH = 8.5 were mixed with 5 mL of the nanorod solution. Finally, 2 mL of AgNO_3 10 mM and 200 μL of ascorbic acid 100 mM were added into the solution under gentle magnetic stirring. The obtained particle dimension was 36.9 ± 5.1 nm \times 30.1 ± 4.9 nm with an aspect ratio of 1.3 ± 0.2 ; see Table 1.

Preparation of Polymer Brushes. Poly(2-vinylpyridine) brushes were prepared on underlying substrates (silicon wafer and glass slide) through the “grafting to” approach, as described elsewhere.⁴² Silicon substrates (2 cm \times 1 cm) were cleaned with ethanol in an ultrasonic bath during 20 min; afterwards, the substrates were immersed in a 1:1:5 mixture of hydrogen peroxide (30%), ammonium hydroxide (29%) and water for 30 min at 60 °C and rinsed with Millipore water

several times. Afterward, a layer thickness of 1.2 ± 0.1 nm of the native oxide layer was measured by means of ellipsometry. A thin layer of PGMA was deposited on the substrates through spin coating from 0.02% w/w solution in chloroform and annealed in a vacuum oven at 100 °C during 20 min. A layer thickness of 2.0 ± 0.1 nm was measured by ellipsometry. At this surface, monocarboxy-terminated poly(2-vinylpyridine) (P2VP-COOH) was spin coated from a 2% w/w solution in chloroform and annealed during 4 h at 150 °C in a vacuum oven. The general process is summarized in Scheme 3. It was investigated that PGMA can serve as a universal anchor for different types of polymer brushes on a wide range of substrates, including silicon, glass, alumina, gold, and silver, due to the high reactivity of the epoxy groups toward hydroxyl groups of these surface.⁴³ The chemical reaction between –COOH groups of carboxy-terminated P2VP brushes and epoxy units of the attached PGMA leads to the chemical attachment of P2VP chains on the underlying substrate. Finally, non-grafted polymer was removed using Soxhlet extraction in chloroform during 4 h. Ellipsometric measurements showed a polymer thickness of 8.2 ± 0.5 nm.

Immobilization of Au and Au@Ag Nanorods onto P2VP Brushes. Metal nanoparticles were immobilized by immersing the P2VP modified silicon wafer substrates into a vial containing 5 mL of the metal colloidal solutions overnight at 28 °C; in all the cases, the concentration of CTAB in the colloidal solution was 0.1 M. Afterward, non or weakly adsorbed particles were removed by rinsing the samples several times with ethanol; see Scheme 3.

For SERS experiments, four different silicon wafers substrates were prepared: in the case of Au-nanorods, P2VP functionalized substrates were immersed in 0.5 and 1.5 mM gold nanorod solutions, denoted here as Au0.5 mM and Au1.5 mM specimens; see Table 1. To prepare the Au0.5 mM system, 10 mL of the previously synthesized Au nanorod solution were centrifuged at 7500 rpm during 1 h, the supernatant was discarded, and the pellet was redispersed in 10 mL of CTAB 0.1 M. To obtain the Au1.5 mM system, 15 mL of the prepared Au nanorod solution was centrifuged at 7500 rpm during 1 h; after removing the supernatant, the precipitated was dispersed in 5 mL of CTAB 0.1 M. For core–shell Au@Ag systems with $R = 2$ and $R = 8$, only the highest particle concentration 1.5 mM was used, and they were denoted AuAg1 and AuAg2, respectively; see Table 1. To prepare the AuAg1 solution, 10 mL of the grown colloidal dispersion were centrifuged at 5000 rpm during 1 h, discarded the supernatant and redispersed in 5 mL of CTAB 0.1 M. The AuAg2 system was prepared adding 5 mL of CTAB 0.1 M to 10 mL of the grown system; the

solution was centrifuged at 5000 rpm during 1 h; the supernatant was removed; and the precipitate was redispersed in 15 mM CTAB 0.1 M.

For UV–vis measurements, only the Au1.5 mM system was prepared on a glass slide substrate cut in a dimension of 4×1 cm, which was functionalized with the same protocol employed for silicon wafers. The P2VP functionalized glass slide was then immersed into a quartz cuvette and was filled with the Au1.5 mM solution overnight at 28 °C. Afterward, non or weakly adsorbed particles were removed by rinsing the samples several times with ethanol.

Preparation of Samples for SERS Measurements. SERS substrates were prepared by immersion of the metal colloidal nanoparticles immobilized on P2VP-functionalized silicon wafers in R6G 10^{-5} M aqueous solution for 2 h; afterward, the samples were cleaned repeatedly with ethanol to remove the nongrafted R6G molecules.

Table 1 describes the nanoparticles used in each study, particle dimension, aspect ratio, concentration of the particles during the immobilization process, the sample code used for the different experiments, and the concentration of Rhodamine 6G for the SERS experiments.

3. RESULTS AND DISCUSSION

Well-defined and homogeneous P2VP brushes were prepared on silicon/glass substrates by exploiting the “grafting to” approach.⁴² The process involves the chemisorption of the PGMA anchoring layer on the oxidized substrates followed by chemical grafting of carboxy-functionalized P2VP chains. Dry thickness was measured as 8.2 ± 0.5 nm. Grafting density of the obtained P2VP brushes was determined to as 0.14 chains/nm² by $\sigma = 1/d_g^2$, where d_g is the distance between two grafting sites, which was derived from $d_g = M_n^{1/2} (N_A d \rho)^{-1/2}$, where M_n is the number average molecular weight of polymer chains, N_A is the Avogadro's number, and ρ (1.18 g/cm³) is the density of P2VP. Because d_g was calculated as 2.64 nm, which is smaller than the radius of gyration of the P2VP polymer coils ($R_g \sim 5$ nm); thus, the polymer layer can be considered as polymer brushes.⁴⁴

Transmission electron microscopy (TEM) images clearly showed the size and the shape of the synthesized gold nanorods. The TEM characterization also proved the core–shell structure of the bimetallic Au@Ag colloidal particles and demonstrates the viability of this silver growth method. As can be observed in Figure 1A, well-defined and large amounts of nanorods with very little contamination by nanospheres were obtained. Figure 1B, C, and D shows representative TEM images of Au@Ag bimetallic particles for AuAg1 and AuAg2 systems. The core–shell structure is readily visible due to mass–thickness contrast already in bright-field images in suitably oriented particles, and further confirmed by elemental mapping using energy filtered images (three-windows method at energy losses of 350 eV, 380 eV, and 450 eV,⁴⁵ Figure 1D). A detailed study of the core–shell particles revealed that the silver is not uniformly distributed over the gold nanorod surface, the morphology of the obtained particles changes from rod to more rounded particles. This morphology change can be also observed in the aspect ratio of the synthesized nanoparticles; see Table 1.

This value was reduced from 2.9, for pure gold nanorods, to 1.3 for the AuAg2 system ($R = 8$). This clearly means that the growth of silver on the gold nanorods takes place preferentially at the lateral sides, as was previously reported for silver growth on gold nanorods in CTAB solutions.⁴⁶

Figure 2 shows UV–vis spectra of the different metal colloidal particles in aqueous solution. In the case of gold nanorods, spectrum A, two plasmon absorption bands can be

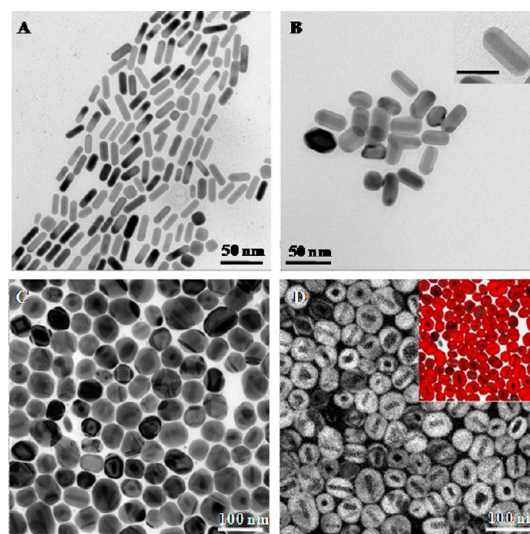


Figure 1. Representative TEM images of the synthesized metal nanoparticles. (A) Gold nanorods, (B) Au@Ag1, $R = 2$, and (C) Au@Ag2, $R = 8$. (D) Energy filtered image of Ag distribution corresponding to area showed in part C. The inset in part D shows the colored overlay of the Ag map over the image part C. The scale bar in the inset of part B is 25 nm.

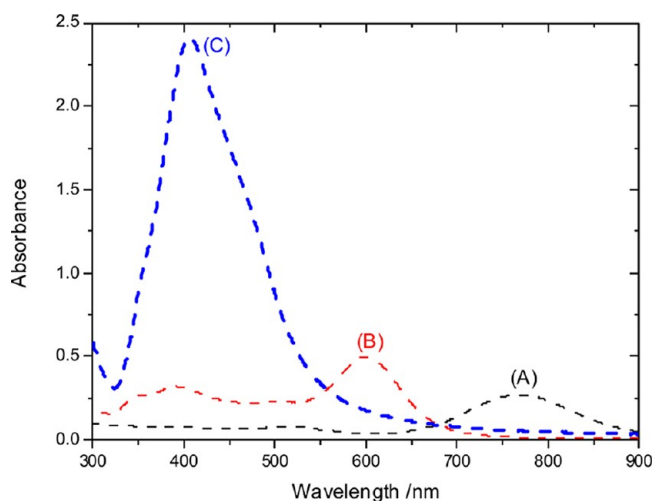


Figure 2. UV–vis spectra of the different metal nanoparticles in aqueous solutions. (A) Gold nanorods, (B) Au@Ag1, and (C) Au@Ag2.

easily observed. The band at lower wavelengths corresponds to the oscillation of the electrons perpendicular to the major axis of the rods and is referred as the localized transverse plasmon band. The band that is red-shifted to higher wavelength is caused by the oscillation of the electrons along the major axis of the nanorods and is known as the localized longitudinal surface plasmon band.^{47,48} The presence of silver in the colloidal system dramatically changed their excitation spectra, as can be seen in spectra B and C in Figure 2, which correspond to UV–vis spectra of the Au@Ag1 and Au@Ag2 systems, respectively.

Both spectra showed a minimum at ca. 320 nm characteristic of the interband transition in the metal that damps the plasma oscillation in this spectral region.⁴⁹ The spectra also revealed the presence of a dipole plasmon resonance at ca. 420 nm attributed to the formation of silver, and as expected, the intensity of this plasmon band increased in the function of the

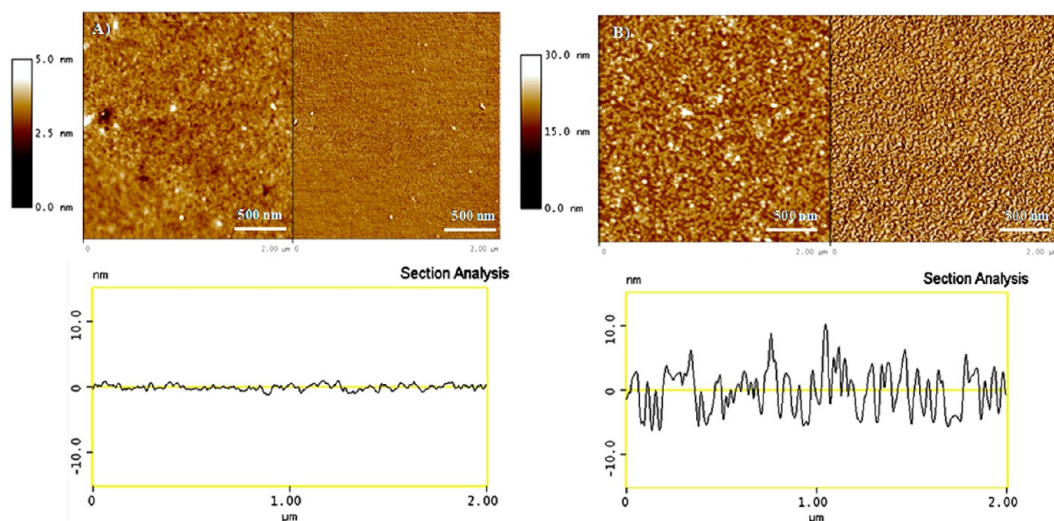


Figure 3. AFM height (left images) and phase (right images) ($2.0 \times 2.0 \mu\text{m}$) and height profile (below) of P2VP brushes (A) before and (B) after the immobilization of gold nanorods.

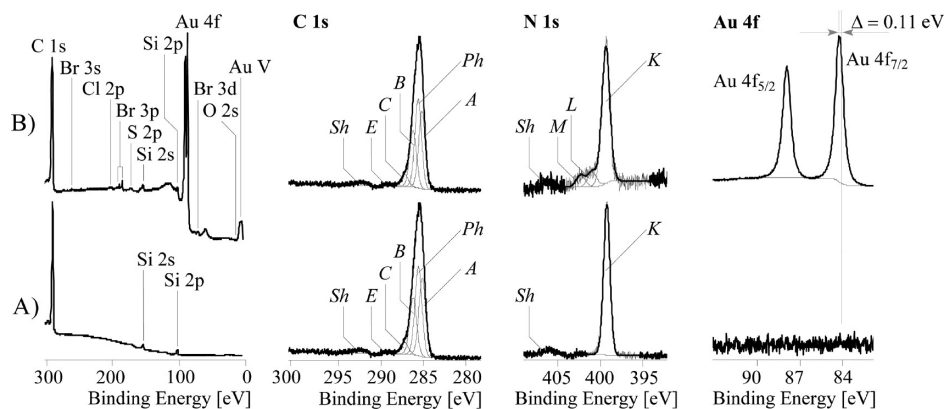


Figure 4. Cut-out of wide-scan XPS spectra (left column) and the relevant high-resolution C 1s, N 1s and Au 4f element XPS spectra recorded from P2VP brush samples without (A) and immobilized (B) gold nanorods. Compared to the peak position of Au 4f_{7/2} spectrum recorded from a 1.0 mm thick gold foil the peak maximum of the Au 4f_{7/2} peak recorded from the immobilized gold nanorods is slightly shifted by $\Delta = 0.11 \text{ eV}$. The difference of this chemical shift is illustrated by the two spaced lines.

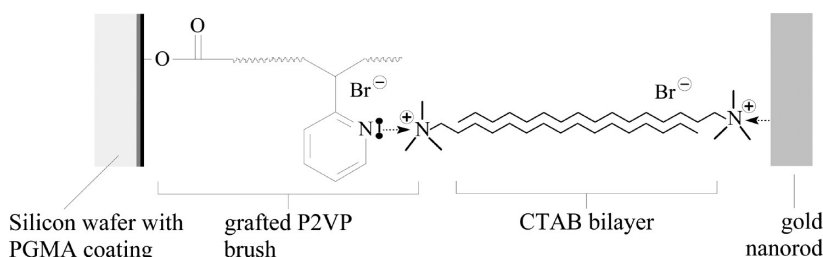
Ag shell. It should be noted that both the transverse and the longitudinal plasmon band drastically blue-shift and acquire higher intensities, principally due to two factors: the higher excitation cross-section of silver and the increase in particle volume. The origin of such a strong variation is assigned to the differences of Ag and Au, which results in a variation of the effective dielectric function of the core-shell nanoparticles.⁵⁰

After the synthesis and the characterization of the metal nanoparticles, the successful immobilization of gold nanorods at P2VP-functionalized substrates was demonstrated by atomic force microscopy (AFM) measurements. For the experiments shown, the concentration of the gold nanorods solution during the deposition process was 1.5 mM. Figure 3 illustrates height and phase AFM images of the P2VP functionalized surface before and after the immobilization of gold nanorods. The morphology of the polymer brushes changed from “carpetlike” to “pebbled one” after the deposition process, confirming the successful immobilization of a dense layer of gold nanorods onto the pH-sensitive polymer brushes. The nanorod deposition can be also confirmed by the height profiles of topographic AFM images of polymer brushes shown in Figure 3, which reveal a significant change in root-mean-square (rms)

roughness of brushes from 0.453 nm before the deposition process to 3.659 nm after the immobilization of gold nanorods.

The presence of Au nanoparticles on polymer brushes has been further evidenced by XPS analysis. Figure 4 represents XPS wide-scan and relevant high-resolution element spectra of the functionalized P2VP silicon wafers without (Figure 4A) and with immobilized gold nanorods (Figure 4B). The wide-scan spectrum of the sample, which was loaded with gold nanorods (Figure 4B), clearly shows the presence of gold (Au 4f peaks and the valence band peak of gold Au V). The atomic concentration of Au on the investigated substrate has been found to be approximately 7.56% by XPS analysis. This value is high compared with that obtained for gold nanospheres attached on pNIPAM brushes.³² They found, also by XPS analysis, 3.69% of Au on the functionalized surface. This difference can be explained taking into account the higher particle concentration used in our case, 1.5 mM instead of 1 mM. The different arrangement capabilities for nanorods compared with nanospheres has also to be considered. It is believed that most of the Au nanoparticles are immobilized on the upper part of the polymer brushes, due principally to steric hindrance caused by the polymer chains, and particles do not

Scheme 4. Schematic Illustration of the Proposed Interaction between the P2VP Brush Grafted on Silicon Wafer and the CTAB-Stabilized Gold Nanorods



penetrate significantly into the brush conformation.⁵¹ The CTAB molecules applied to stabilize the gold nanorods introduced bromine, which was analyzed as Br 3d and Br 3p peaks. The high-resolution C 1s spectra of the two P2VP brush samples did not show significant differences in their shapes. They were deconvoluted into three intensive component peaks, A, Ph, and B, appearing from the constituents of the P2VP polymer. Component peak A shows saturated hydrocarbons ($C_{6}H_{12}$) forming the polymer backbone ($-CH_2-CH-$). Carbon atoms of the pyridine ring, which are not bonded to nitrogen contributed to component peak Ph. Their chemical shift to values higher than 285 eV results from the electron affinity of nitrogen atom in the pyridine ring and the endeavor of the π -electron system to compensate the nitrogen's $-I$ effect by a homogeneous distribution of the electron density in the π -electron system. Carbon atoms of the conjugated $=C-N=C- \leftrightarrow -C=N-C=$ bonds, which shows a significantly higher chemical shift were identified as component peak B.⁵² The binding energy of the two nitrogen-bonded carbon atoms was not different. The intensity ratios of the two component peaks Ph and B correspond to the expected ratio of $[Ph]/[B] = 3:2$. The intensities of component peaks A were slightly increased because small amounts of surface contaminations contributed to these component peaks. To fit the C 1s spectra well, the introduction of two additional components of peaks C and E was necessary. Component peak E presents carboxy carbon atoms of carbonic ester groups ($O=C-O-C-$), which were formed during the grafting of the P2VP-COOH polymers on the PGMA-coated silicon wafer. The more intensive component peak C shows the $C-O$ bond of alcoholic groups ($-C-OH$), ether groups ($-C-O-C-$) and alcoholic sided carbon atoms of the ester groups ($O=C-O-C-$). These functionalities are also typical reaction products of grafting reaction.

In the region of about 292 eV, shakeup peaks (Sh) were observed. They result from electron transitions from $\pi \rightarrow \pi^*$ orbitals taking place in the conjugated π -electron systems of the pyridine groups. The N 1s spectrum recorded from the P2VP brush sample shows only one component peak K appearing from nitrogen atoms involved in the pyridine rings. Their participation on the delocalized π -electron systems leads to shakeup peaks discussed above. After the deposition of the gold nanorods, two further component peaks (L and M) were observed in the N 1s spectrum. The binding energy of component peak M (BE \approx 402 eV) is very typical for organic ammonium salts, such as the charge-carrying group of the CTAB molecules ($-CH_2-N^+[CH_3]_3$). The immobilization of gold nanorods was carried out at pH \approx 7, which is above the isoelectric point of P2VP. Hence, pyridine groups were deprotonated and did not contribute to component peak

M.³⁷ The binding energy of component L (BE \approx 400 eV) suggest the presence of amine-bonded nitrogen atoms. However, such groups are not expected in samples, which were investigated. We suppose that the origin of the component L is the quaternized nitrogen atom presented in the CTAB molecule, which is strongly interacting with the gold surface. During the interaction, the positive charge remains stable on the nitrogen of the ammonium group but electrons provided by gold atoms are able to compensate the field of the positive charge. Hence, the net charge controlling chemical shift in the N 1s XPS spectrum appears decreased for the CTAB/gold interaction pairs, and the binding energy of component peak L corresponds to the binding energy usually found for electrically neutral amino groups. Our assumption is supported by a small chemical shift, which was observed in the corresponding Au 4f_{7/2} spectrum. The compensation of the positive charges of the interacting CTAB molecules increased the binding energy from 84.00 eV, which was expected for metallic gold to 84.11 eV showing the decreased electron density on the interacting gold atoms (Δ in the Au 4f spectrum in Figure 4B). Taking into account that the CTAB molecules form a bilayer on the gold nanorod surface, where each second ammonium group is localized on the gold surface,⁵³ the intensities of the component peaks L and M should be equal. In fact, the $[L]/[M]$ ratio was $[L]/[M] = 1.2$, showing a small excess of the charged-neutralized species. Unfortunately, neither the N 1s spectrum nor the Au 4f spectrum gave a hint on coordinative bonds between the P2VP polymer and the CTAB-coated gold nanorods. In virtue of the analyzed XPS spectra, we propose a commonly surfactant-like interaction between the outer ammonium groups of the CTAB layer, which covers the gold nanorod surfaces and the polar pyridine groups of the P2VP brushes. The n -orbital of the pyridine nitrogen is able to provide its nonbonded electrons to for the interaction with the ammonium head groups of the CTAB molecules. Ammonium groups having a decreased net charge also contribute to component peak L in the corresponding N 1s spectrum. The interaction mechanism is schematically shown in Scheme 4.

As was previously mentioned, P2VP brushes, as weak polyelectrolytes, shows pH-responsive behavior and has an isoelectric point (IEP) of pH = 6.³⁷ At pH 2, the pyridine groups of the polymer chains are highly protonated, and an increase of the electrostatic repulsions between the positive charges causes stretch in the polymer chain. As the pH of the solution increases above the IEP, the deprotonation of the pyridine groups causes that the P2VP layer undergoes hydrophobic collapse from the swollen to nearly solvent-free state.³⁴ Here, this pH-responsive behavior was used to fabricate a nanosensor device exploiting the tunable optical properties of

the metal nanoparticles. UV–vis experiments at two different pHs, pH 2 and pH 6, were carried out on P2VP-functionalized glass slides, which were immersed into a gold nanorod solutions at $[Au] = 1.5 \text{ mM}$. Figure 5 shows UV–vis spectra of gold

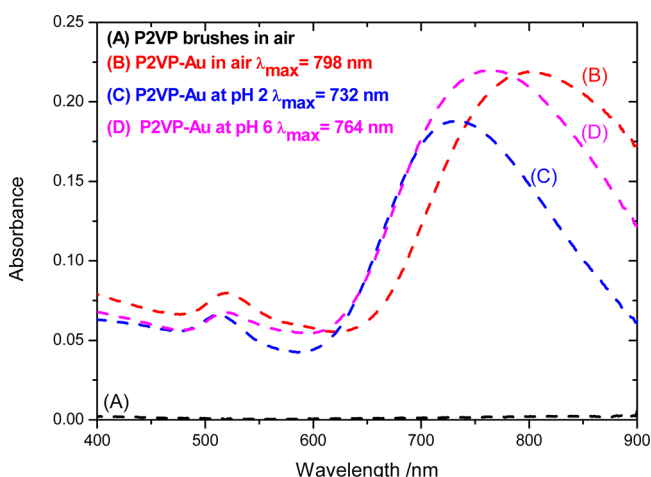


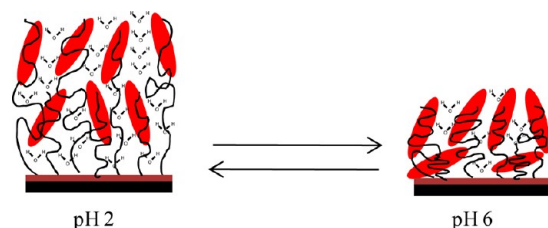
Figure 5. UV–vis spectra of the different glass slides substrates: (A) bare P2VP brushes, (B) Au nanorods on P2VP brushes in air, (C) Au nanorods on P2VP brushes in water at pH 2, and (D) Au nanorods on P2VP brushes in water at pH 6.

nanorods immobilized onto P2VP brushes in aqueous solution at two mentioned pH values, and in dry state. The UV–vis spectrum of the bare P2VP brushes is also included. As can be seen, no absorption band for the bare P2VP brushes in a dry state was observed, spectrum A. Two absorptions bands at 518 and 798 nm, which correspond with the transverse and longitudinal plasmon band, respectively, were observed for the Au nanorods immobilized on P2VP brushes in a dry state, spectrum B, which proves the presence of Au nanoparticles on the polymer brushes.

If we compare the UV–vis spectra of the Au functionalized substrate at pH 2 and 6, spectra C and D, respectively, a red-shift of 32 nm in the longitudinal localized plasmon band caused by the different chain conformation at the investigated two different pH values. This important shift can be explained according to two different effects. First, during the swelling–deswelling process, induced by the different pH, a significant change in the refractive index within the polymer chains is produced.⁵⁵ As Mie’s theory establishes, changes in the refractive index surrounding metal nanoparticles produce a displacement in the plasmon band.^{7,56,57} This assumption is also evidenced with the shift observed in the UV–vis spectrum of the immobilized Au nanorods on P2VP brushes in air. A displacement in the longitudinal plasmon band of 34 nm between both collapsed states is observed. This shift is also attributed to the variation in the surrounding media from water to air. The second effect to be considered in the plasmon displacement is the fact that P2VP brushes swell in aqueous media at pH 2, resulting in an increase in interparticle distance of immobilized nanorods. It is well-known from literature that an increase in interparticle distance of metal nanoparticles leads to a blue-shift in the plasmon position.^{58,59} Consequently, particles are closer, and the interparticle distances decrease in the collapsed state of the P2VP brushes at pH 6, and in the dry state, causing a significant red-shift in the plasmon position and a slight broadening in the absorption band.³² A schematic

illustration of the swelling–deswelling behavior of P2VP brushes with immobilized Au nanorods at two different pH values is shown in Scheme 5. As can be observed, both effects are represented. As is shown, the local refractive index surrounding gold nanorods at pH 2 is greater than that at pH 6.

Scheme 5. Schematic Illustration of the Swelling–Deswelling Process of P2VP-Aurod Brushes in Water at pH 2 and pH 6^a



^aDifferent refractive indexes and interparticle distances are shown.

The amount of water molecules within the polymer brushes is higher at pH below its IEP; thereby, a displacement in absorption peak is expected. This plasmon displacement is consistent with that previously reported for gold nanorods encapsulated with PNIPAM microgels, where a swelling–deswelling process in a core–shell Aurod@pNIPAM nano-hybrid system produced a displacement in the longitudinal plasmon band about 30 nm. This displacement was explained due to differences in the refractive index around the Nrod core between the swollen and the collapsed state.⁶⁰ In Scheme 5, a decrease in interparticle distance caused by the collapse of polymer chains is also shown. This interparticle decrease also contributes to the remarkable red-shift in the plasmon band position and to the broadening of the absorption band. Previous work regarding spherical gold nanoparticles immobilized on poly(N-Isopropylacrylamide) polymer brushes showed a displacement of 12 nm between the swollen and the collapsed state.³² It should also be pointed out, that this larger plasmon displacement of 32 nm is mainly caused by a higher electromagnetic field concentration in nanorods compared to the spheres, which also leads to a higher sensitivity toward local refractive index changes, improving notably the potential application of this nanoassembly as highly sensitive nanosensor. With the aim to study the SERS capabilities that both the Au and Au@Ag nanoparticles supply to the system, four different P2VP-functionalized silicon wafers with attached metal nanoparticles were investigated; see Table 1. Figure 6 shows representative SEM images of the four nanoassemblies studied; Au0.5 mM, Au1.5 mM, AuAg1, and AuAg2. Figure 6A and B represents SEM images of the Au0.5 mM and Au1.5 mM systems, respectively. In the case of the lower particle concentration, a homogeneous distribution of gold nanorods with a low amount of plasmon coupling was observed. Aggregation free surfaces can be observed due to the particles are stabilized with CTAB. This charged quaternary ammonium salt forms a bilayer on the metal surface, which stabilizes the system during the deposition process by electrostatic interactions. As was mentioned in the introduction, plasmon coupling is produced when particle distance among metal nanoparticles range between zero interparticle distance and ~ 2.5 times the particle size,²³ within this areas a remarkably enhanced in the SERS effect is produced. In Figure 6B, on the contrary, homogeneous distribution of particles and significant

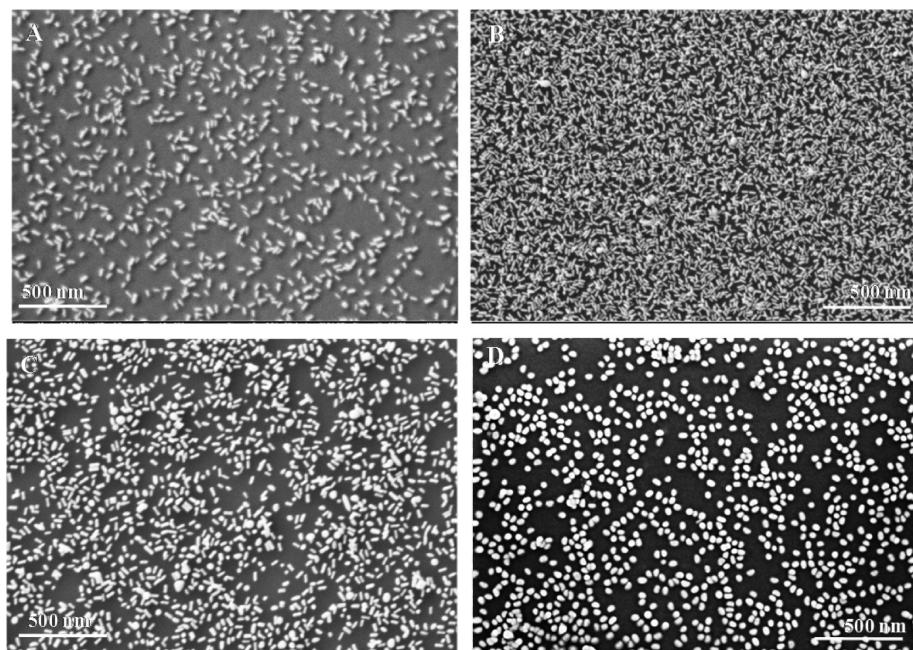


Figure 6. Representative scanning electron microscopy (SEM) images of P2VP modified silicon wafers immersed into different aqueous solution of metal nanoparticles. (A) Au0.5 mM; (B) Au1.5 mM; (C) AuAg1, and (D) AuAg2.

plasmon coupling were obtained with the Au1.5 mM system. Due to this large amount of coupling, this particle concentration was used in the experiments for bimetallic Au@Ag nanoparticles, shown in Table 1. Figure 5C and D show SEM images for the AuAg1 and AuAg2 systems, respectively. As can be seen, homogeneous distribution and plasmon coupling was also reached on these brush systems. To compare the effectiveness of the different substrates in SERS spectroscopy, Rhodamine 6G (R6G) was used as model analyte. Figure 7 shows the 532 nm excitation SERS spectra of $1.0 \times$

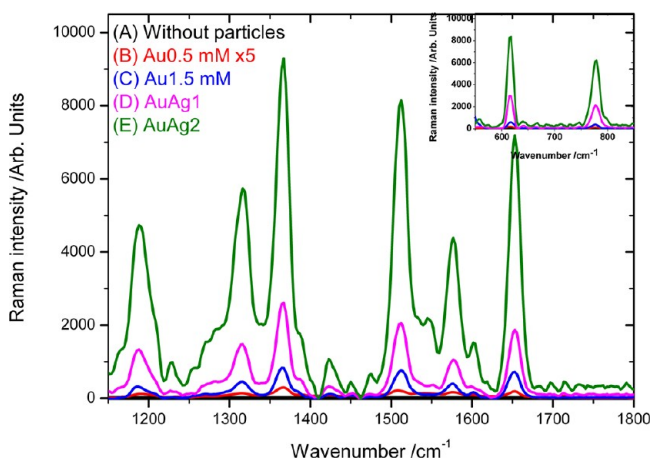


Figure 7. Raman spectra of R6G (10^{-5} M) aqueous solution adsorbed on the different samples tested: (A) P2VP brushes without particles, (B) Au 0.5 mM, (C) Au1.5 mM, (D) AuAg1, and (E) AuAg2.

10^{-5} M R6G on the four different samples and for a substrate without immobilized particles. The spectrum of the Au0.5 mM system was multiplied by 5 for a better comparison. All spectra were smoothed by Savitzki–Golay method, and the baseline was corrected for the elimination of the fluorescence background between 1065 and 1780 cm^{-1} by polynomial function

seventh order. In all the specimens, except for that without immobilized metal nanoparticles, the SERS effect was observed, showing clear Raman peaks of R6G, including the peaks at 615, 779, as shown in the inset of Figure 7, and the peaks at 1189, 1316, 1365, 1510, 1577, and 1652 cm^{-1} , within the spectral region from 1200 up to 1800 cm^{-1} , which is closely in agreement with findings in the literature.⁶¹ As can be seen in spectra B and C, for Au0.5 mM and Au1.5 mM systems, respectively, the SERS intensity increases with the concentration of particle deposited on the brushes. Apart from the concentration of particle, a significant increase in the SERS signal was found when silver was present in the system. As expected, this enhancement depended remarkably on the thickness of the silver shell, as the thicker the silver shell, the higher the SERS intensity was; see spectra D and E for specimens Au@Ag1 and Au@Ag2, respectively. This enhancement can be explained considering the more intense surface plasmon for silver nanoparticles compared to gold nanoparticles,¹⁰ proving the importance of this metal for SERS applications.

Enhancement factors (EFs) were determined to quantify the potential uses of these nanoassemblies for SERS spectroscopy and to be compared with other approaches. EFs of probe molecules are usually calculated using the general eq 1:⁶²

$$EF = \frac{I_{\text{SERS}}}{I_{\text{Raman}}} \frac{N_{\text{Raman}}}{N_{\text{SERS}}} \quad (1)$$

where I_{Raman} and I_{SERS} mean the corresponding normal Raman and SERS intensities of R6G at 1365 cm^{-1} , and N_{Raman} and N_{SERS} denote the number of R6G molecules, which contribute to the signal intensity, regular Raman and enhanced system, respectively. Rhodamine 6G is a fluorescent molecule that adsorbs strongly with a maximum at 528 nm, close to the laser excitation we used for Raman measurements (532 nm). Thereafter, the experimental Raman scattering spectrum is difficult to obtain because of the overwhelming fluorescent background obtained at 532 nm. In the present work, for the

SERS enhancement factor calculations, we used the estimation reported by Zhou et al.¹⁴ They consider, under the same experimental conditions, the relationship of the R6G signal intensity between the normal Raman scattering I_{Raman} and the fluorescence I_{Flu} as

$$\text{EF} = \frac{I_{\text{Raman}}}{I_{\text{Flu}}} = \frac{\sigma_{\text{Raman}}}{\sigma_{\text{Flu}}} = \frac{10^{-25}}{10^{-16}} = 10^{-9} \quad (2)$$

where σ_{Raman} and σ_{Flu} are the cross sections of the normal Raman scattering and the fluorescence at 514.5 nm, 10^{-25} and 10^{-16} cm²/sr, respectively.^{63,64} Therefore, enhancement factors were calculated using the formula

$$\text{EF} = \frac{I_{\text{SERS}}}{I_{\text{Flu}}} \frac{N_{\text{Raman}}}{N_{\text{SERS}}} \times 10^9 \quad (3)$$

N_{Raman} and N_{SERS} can be easily calculated with the assumption that the density of R6G molecules per surface area is the same at unenhanced and enhanced conditions:

$$\frac{N_{\text{Raman}}}{N_{\text{SERS}}} = \frac{\text{Raman area}}{\text{metal surface area}} \quad (4)$$

For P2VP brushes without metal nanoparticles, the effective area that contributes to the Raman signal is equal to that of the laser spot area (1 μm^2), while for P2VP brushes with immobilized metal nanoparticles the effective area that contributes to the SERS signal is the surface area of the incorporated nanoparticles. This value can be calculated taking into account the total number of particles within 1 μm^2 . This value was determined using particle detection routines in Scandium Software (Olympus Soft Imaging Solutions GmbH) in each case. So, the total metal surface area can be calculated multiplying the previously calculated total number of particles per μm^2 by the surface area of 1 particle, determined by the formula $S = 2\pi r(h + r)$. For example, for the AuAg2 system, the calculated total number of particles per μm^2 was 232. This value is multiplied by the surface area of 1 metal nanoparticle (4.91×10^{-3} μm^2), obtaining a total surface area of 1.14 μm^2 . Therefore, the maximum $N_{\text{Raman}}/N_{\text{SERS}}$ factor to be introduced in eq 3 is $1/1.14 = 0.87$. Table 2 summarizes the particle

Table 2. Sample, Particle Dimension, Number of Particles per μm^2 , Surface Area of 1 Particle, Metal Surface Area per μm^2 , and Maximum $N_{\text{Raman}}/N_{\text{SERS}}$ for All the Samples Tested for EF Calculation

sample	particle dimension, nm	no. of metal particles per μm^2	surface area of 1 particle, μm^2	total metal surface area (μm^2) per μm^2	max $N_{\text{Raman}}/N_{\text{SERS}}$
AuO.5 mM	31.7×11.2	402	1.29×10^{-3}	0.516	1.93
Au1.5 mM	31.7×11.2	1250	1.29×10^{-3}	1.61	0.62
AuAg1	35.0×17.8	432	2.45×10^{-3}	1.06	0.94
AuAg2	36.9×30.1	232	4.91×10^{-3}	1.14	0.87

dimension, the number of particles per μm^2 , the surface area of 1 particle, the total surface area of metal nanoparticles per μm^2 , and the maximum $N_{\text{Raman}}/N_{\text{SERS}}$ in each studied case. In the SEM images showed in Figure 6, a homogeneous distribution of particles was observed, so we can assume that the number of particles per area is highly uniform within the irradiated area.

A further important consideration has to be taken into account in every SERS experiment, as not all the R6G molecules can contribute to the SERS effect because in Raman spectroscopy, only 180° backscattering molecules are detected. In previous works about EFs estimations,^{15,16} nanoparticles embedded on the different patterns were simplified as hemispheres on a flat substrate, and thus, only 50% of R6G molecules can contribute to the SERS effect. In our case, metal nanorods have been immobilized on a flat surface.

Figure 8 shows a schematic representation of a gold nanorod distribution with incorporated R6G molecules distributed at the

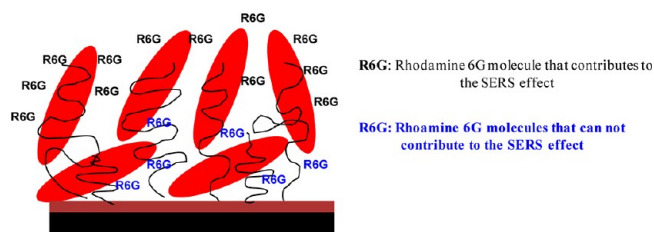


Figure 8. Schematic representation of the R6G distribution into the nanoparticles system.

nanoparticle surface. We have estimated that approximately 60% of R6G molecules can contribute to the SERS signal (molecules in black color), due to a possible tilting of certain metal nanorods on the P2VP brushes, whereas 40% of R6G can not contribute to the SERS signal (molecules in blue color).

After this consideration, Table 3 summarizes the SERS and fluorescence intensity at 1365 cm^{-1} , the maximum EF and the

Table 3. Sample Used in the Experiments, SERS and Fluorescence Intensity at 1365 cm^{-1} , Maximum Calculated EF and Estimated EF for the Different Specimens Used in the Measurements

sample	I_{SERS}	I_{Flu}	max. EF	est. EF
AuO.5 mM	58	32	3.5×10^9	2.1×10^9
Au1.5 mM	832	32	1.6×10^{10}	9.7×10^9
AuAg1	2586	32	7.6×10^{10}	4.6×10^{10}
AuAg2	9035	32	2.8×10^{11}	1.7×10^{11}

estimated EF in each system using eq 3. As can be observed in Table 3, for gold nanorods the EFs depend on the particle concentration and increases from 2.1×10^9 to 9.7×10^9 for the samples AuO.5 mM and Au1.5 mM, respectively. Therefore, SERS intensity clearly depends on the concentration of particles; however, as was previously explained, this dependence is not only due to the increase in the number of enhancement points but also because at a particle concentration 1.5 mM more plasmon coupling is generated, which further enhances the Raman signal, compare Figure 6A and B. An additional increase of the EF is produced when silver is deposited around the gold surface. As was expected, this enhancement is proportional to the thickness of the silver shell and increases from 4.6×10^{10} to 1.7×10^{11} for Au@Ag1 and Au@Ag2 specimens, respectively. This enhancement is produced because the plasmon intensity and, in consequence, the SERS effect increases with the particle diameter.^{65,66} These values have the same order of magnitude as EFs previously reported for the fabrication of SERS substrates using different approaches, as ion exchange process, layer by layer assembly, or thermal vapor deposition,^{15,16,67} proving that these P2VP-Au@Ag nano-

assemblies are sensitive enough to be implemented as effective plasmonic substrates for SERS applications.

4. CONCLUSIONS

We have developed an easy and reproducible strategy for the immobilization of Au and Au@Ag nanorods onto macroscopic substrates containing pH-responsive P2VP polymer brushes. These resulting nanoassemblies can be used as pH-sensitive nanosensors by exploiting both the pH induced swelling–deswelling properties of polymer brushes and the tunable optical properties of Au nanoparticles. The presence of nanorods in the system improved remarkably the optical responses of the nanoassembly compared with other morphologies previously studied. An important shift in the longitudinal plasmon band between the swollen and collapsed states was observed and offers the possibility to fabricate tunable optical devices composed by other stimuli-responsive polymer brushes, as temperature responsive poly(N-Isopropylacrylamide) brushes or solvent sensitive polystyrene brushes.

Two different controllable silver shells were successfully grown on the gold nanorod surface with the aim to investigate the SERS responses. The presence of the silver shell and the core–shell Au@Ag structure was confirmed by UV–vis spectroscopy and TEM images. AFM images and XPS analysis confirmed the presence of metal nanoparticles on the functionalized substrates. The SERS intensities for the different nanoassemblies (Au nanorods at two different particle concentrations and Au@Ag with two different silver shells) were investigated, and it was found that all the specimens presented SERS responses. A significant increase in the SERS intensity was observed when silver was present in the structure. The SERS signal depended on both the particle concentration on the irradiated surface and the thickness of the silver shell surrounding the gold nanorod surface. Enhancement factors on the order of 10^{11} were calculated for the specimen with the thicker silver shell. This value demonstrates the potential application of these 2D devices in the detection of SERS-active molecules for application in SERS spectroscopy.

AUTHOR INFORMATION

Corresponding Author

*E-mail: Uhlmannp@ipfdd.de.

Notes

The authors declare no competing financial interest.

ACKNOWLEDGMENTS

The authors acknowledge financial support from DFG (SPP 1369/2, project STA 324/37-2 and STA 324/49-1) and the state of Saxony (SMWK 4-7531. 50-03-843-12/1). The authors are thankful to Mr. Soumyadip Choudhury for helping with AFM analyses.

REFERENCES

- Hutter, E.; Fendler, J. H. *Adv. Mater.* **2004**, *16*, 1685–1706.
- Jain, J. K.; El-Sayed, I. H.; El-Sayed, M. A. *Nano Today* **2007**, *2*, 18–29.
- Ipe, B. I.; Thomas, K. G.; Barazzouk, S.; Hotchandani, S.; Kamat, P. V. *J. Phys. Chem. B* **2002**, *106*, 18–21.
- Caseri, W. *Macromol. Rapid Commun.* **2000**, *21*, 705–722.
- Kreibig, U.; Vollmer, M. *Optical Properties of Metal Clusters*; Springer: Berlin, Germany, 1995.
- Link, S.; El-Sayed, M. A. *Int. Rev. Phys. Chem.* **2000**, *19*, 409–453.
- Mie, G. *Ann. Phys.* **1908**, *25*, 329.
- Fleischmann, M.; Hendra, P. J.; McQuillan, A. J. *Chem. Phys. Lett.* **1974**, *26*, 163–166.
- Moskovits, M. *Rev. Mod. Phys.* **1985**, *57*, 783–826.
- Johnson, P. B.; Christy, R. W. *Phys. Rev. B* **1975**, *11*, 1315–1323.
- Xu, H.; Bjerneld, E. J.; Käll, M.; Borjesson, L. *Phys. Rev. Lett.* **1999**, *83*, 4357–4360.
- Gunnarsson, L.; Bjerneld, E. J.; Xu, H.; Petronis, S.; Kasemo, B.; Käll, M. *Appl. Phys. Lett.* **2001**, *78*, 802–804.
- Glass, R.; Arnold, M.; Blümmel, J.; Küller, A.; Möller, M.; Spatz, J. P. *Adv. Funct. Mater.* **2003**, *13*, 569–575.
- Zhou, J.; Xu, S.; Xu, W.; Zhao, B.; Ozaki, Y. *J. Raman Spectrosc.* **2009**, *40*, 31–37.
- Karvonen, L.; Chen, Y.; Säynätjoki, A.; Taivola, K.; Tervonen, A.; Honkanen, S. *Opt. Mater.* **2011**, *34*, 1–5.
- Chen, Y.; Jaakola, J. J.; Säynätjoki, A.; Tervonen, A.; Honkanen, S. *J. Raman Spectrosc.* **2011**, *42*, 936–940.
- Ung, T.; Liz-Marzán, L. M.; Mulvaney, P. *Colloids Surf. A* **2002**, *202*, 119–126.
- Malikova, N.; Pastoriza-Santos, I.; Schierhorn, M.; Kotov, N. A.; Liz-Marzán, L. M. *Langmuir* **2002**, *18*, 3694–3697.
- Bandyopadhyay, K.; Patil, V.; Vijayamohan, K.; Satry, M. *Langmuir* **1997**, *13*, 5244–5248.
- Gao, F.; Lu, Q. Y.; Komarneni, S. *Chem. Mater.* **2005**, *17*, 856–860.
- Ghosh, S. K.; Pal, T. *Chem. Rev.* **2007**, *107*, 4797–4862.
- Zhou, Q.; Li, X.; Fan, Q.; Zhang, X.; Zheng, J. *Angew. Chem., Int. Ed.* **2006**, *45*, 3970–3973.
- Su, K. -H.; Smith, S.; Schultz, S. *Nano Lett.* **2003**, *3*, 1087–1090.
- Huang, X. H.; Neretina, S.; El-Sayed, M. A. *Adv. Mater.* **2009**, *21*, 4880–4910.
- Jain, P. K.; Eustis, S.; El-Sayed, M. A. *J. Phys. Chem. B* **2006**, *110*, 18243–18253.
- Huang, X.; El-Sayed, I. H.; Qian, W.; El-Sayed, M. A. *Nano Lett.* **2007**, *7*, 1591–1597.
- Milner, S. T. *Science* **1991**, *251*, 905–914.
- Brittain, W. J.; Minko, S. *J. Polym. Sci., Part A: Polym. Chem.* **2007**, *45*, 3505–3512.
- Zhao, B.; Brittain, W. J. *Prog. Polym. Sci.* **2000**, *25*, 677–710.
- Burkert, S.; Bittrich, E.; Kuntzsch, M.; Müller, M.; Eichhorn, K. J.; Bellmann, C.; Uhlmann, P.; Stamm, M. *Langmuir* **2010**, *26*, 1786–1795.
- Liu, Z.; Pappacena, K.; Cerise, J.; Kim, J.; Durning, C. J.; ÓShaughnessy, B.; Levicky, R. *Nano Lett.* **2002**, *2*, 219–224.
- Gupta, S.; Agrawal, M.; Uhlmann, P.; Simon, F.; Stamm, M. *Chem. Mater.* **2010**, *22*, 504–509.
- Gupta, S.; Uhlmann, P.; Agrawal, M.; Chapuis, S.; Oertel, U.; Stamm, M. *Macromolecules* **2008**, *41*, 2874–2879.
- Tokareva, I.; Minko, S.; Fendler, J. H.; Hutter, E. *J. Am. Chem. Soc.* **2004**, *126*, 15950–15951.
- Chen, H.; Kou, X.; Yang, Z.; Ni, W.; Wang, J. *Langmuir* **2008**, *24*, 5233–5237.
- Biesalki, M.; Johannsmann, D.; Ruhe, J. *J. Chem. Phys.* **2002**, *117*, 4988–4994.
- Houbenov, N.; Minko, S.; Stamm, M. *Macromolecules* **2003**, *36*, 5897–5901.
- Lemieux, M.; Usov, D.; Minko, S.; Stamm, M.; Shulha, H.; Tsukruk, V. V. *Macromolecules* **2003**, *36*, 7244–7255.
- Minko, S.; Patil, S.; Datsyuk, V.; Simon, F.; Eichhorn, K. J.; Motornov, M.; Usov, D.; Tokarev, I.; Stamm, M. *Langmuir* **2002**, *18*, 289–296.
- Nikoobakht, B.; El-Sayed, M. A. *Chem. Mater.* **2003**, *15*, 1957–1962.
- Yang, Z.; Lin, Y.-W.; Tseng, W.-L.; Chang, H.-T. *J. Mater. Chem.* **2005**, *15*, 2450.
- Ionov, L.; Stamm, M.; Diez, S. *Nano Lett.* **2006**, *6*, 1982.
- Luzinov, I.; Iyer, K. S.; Klep, V.; Zdyrko, B.; Draper, J.; Liu, Y. *Polym. Prepr.* **2003**, *44*, 437.

- (44) Zdyrko, B.; Klep, V.; Luzinov, I. *Langmuir* **2003**, *19*, 10179.
- (45) Egerton, R. F. *Electron Energy-Loss Spectroscopy in the Electron Microscope*, 2nd ed.; Plenum Press: New York, 1996.
- (46) Cho, P. H. C.; Camargo, Y. X. *Adv. Mater.* **2010**, *22*, 744.
- (47) Yu, Y.; Chang, S.; Lee, C.; Wang, C. R. C. *J. Phys. Chem. B* **1997**, *101*, 6661.
- (48) Link, S.; Mohamed, M. B.; El-Sayed, M. A. *J. Phys. Chem. B* **1999**, *103*, 3073.
- (49) Kreibig, U.; Vollmer, M. *Optical Properties of Metal Clusters*, Springer Series in Materials Science, Vol.25; Springer-Verlag: Weinheim, Germany, 1995.
- (50) Liu, M.; Guyot-Sionnest, P. *J. Phys. Chem. B* **2004**, *108*, 5882.
- (51) Gupta, S.; Agrawal, M.; Uhlmann, P.; Simon, F.; Oertel, U.; Stamm, M. *Macromolecules* **2008**, *41*, 8152.
- (52) Beamson, G.; Briggs, D. *High-Resolution XPS of Organic Polymers: The Scienta ESCA300 Database*; John Wiley & Sons: Chichester, U.K., 1992.
- (53) Alkilany, A. M.; Frey, R. L.; Ferry, J. L.; Murphy, C. J. *Langmuir* **2008**, *24*, 10235. (61) . (62) . (63) (64) . (65) . (66) (67)
- (54) Ionov, L.; Sapra, S.; Synyska, A.; Rogach, A.; Stamm, M.; Diez, S. *Adv. Mater.* **2007**, *23*, 7472.
- (55) Mitsuishi, M.; Koishikawa, Y.; Tanaka, H.; Sato, E.; Mikayama, T.; Matsui, J.; Miyashita, T. *Langmuir* **2007**, *23*, 7472.
- (56) Liz-Marzán, L. M.; Giersig, M.; Mulvaney, P. *Langmuir* **1996**, *12*, 4329.
- (57) Pérez-Juste, J.; Pastoriza-Santos, I.; Liz-Marzán, L. M.; Mulvaney, P. *Coord. Chem. Rev.* **2005**, *249*, 1870.
- (58) Takeuchi, Y.; Ida, T.; Kimura, K. *Surf. Rev. Lett.* **1996**, *123*, 8197.
- (59) Kreibig, U.; Genzel, L. *Surf. Sci.* **1985**, *156*, 678.
- (60) Contreras-Cáceres, R.; Pastoriza-Santos, I.; Álvarez-Puebla, R. A.; Pérez-Juste, J.; Fernández-Barbero, A.; Liz-Marzán, L. M. *Chem. Eur. J.* **2010**, *16*, 9462.
- (61) Hildebrandt, P.; Stockburger, M. *J. Phys. Chem.* **1984**, *88*, 5935.
- (62) Alvarez-Puebla, R.; Santos, D. S.; Aroca, R. F. *Analyst* **2007**, *132*, 1210.
- (63) Nie, S.; Emory, S. R. *Science* **1997**, *275*, 1102.
- (64) Asher, S. A. *Annu. Rev. Phys. Chem.* **1988**, *39*, 537.
- (65) Veronica-Rigo, M.; Seo, J.; Kim, W.-J.; Jung, S. *Vibration. Spec.* **2011**, *57*, 315.
- (66) Rodríguez-Fernández, J.; Pérez-Juste, J.; García de Abajo, F. J.; Liz-Marzán, L. M. *Langmuir* **2006**, *22*, 7007.
- (67) Gupta, R.; Weimer, W. A. *Chem. Phys. Lett.* **2003**, *374*, 302.